

Direct determination of electron and hole temperatures from continuous-wave photoluminescence measurement

Thomas Vezin,* Nathan Roubinowitz,[†] Laurent Lombez,[‡] Jean-François Guillemoles,[†] and Daniel Suchet[†]
(Dated: September 5, 2024)

Hot-carrier solar cells offer potential for enhancing the energy-conversion efficiency of photovoltaic devices, but their design and operation require a good assessment of carrier temperatures. Electrons and holes may have different temperatures, for instance because of their effective mass mismatch in III-V compounds. We propose a purely optical method which allows the direct and distinct estimation of electron and hole temperatures in steady state. This technique, based on photoluminescence, relies on the precise determination of the band-filling signature. We apply this technique to an InGaAsP single quantum well. Electron temperature surpasses 1000 K at largest excitation intensity, while holes remain colder, close to lattice temperature. Nonetheless, the increase in hole temperature is too large to be explained purely by photon absorption, which demonstrates an energy transfer from electrons to holes.

I. INTRODUCTION

Hot carrier solar cells (HCSC) hold promise to increase the energy-conversion efficiency of solar cells close to the thermodynamic limit of 86% [1]. Absorption of high energy photons promotes electrons and holes with excess kinetic energy. Carrier-carrier interactions allow the system to relax towards thermal states with high temperatures and chemical potentials at a subfemtosecond scale [2]. These hot carriers then cool down to lattice temperature, typically in a few ps [3]. By finding materials with lower thermalization rates, such as III-V quantum wells (QW) [4], it is possible to maintain carriers at high temperatures in steady-state. This excess temperature can be used to boost the voltage of the solar cell [1, 5–7].

However electrons and holes are likely to have different temperatures for several reasons, summarized schematically on Fig. 1. First, due to their mass mismatch, the energy of the absorbed photon is unevenly distributed among them. The same argument applies to the distribution of the radiated power, and to the carrier-LO phonon coupling – which was found to be the main thermalization mechanism in non-polar III-V materials [8, 9]. By contrast, carrier-carrier interactions will tend to equate the population temperatures. The temperatures reached in steady-state will result from the trade-off between all these contributions. As a consequence, many investigations in the 80s and 90s tried to distinguish electron and hole temperatures in III-V materials.

This investigation was first done with numerical simulations [10], which showed that electrons should be ther-

malized at a higher temperature than holes for a few picoseconds, due to weak electron-hole interaction. After this, many models including different temperatures for electrons and holes were developed, to include a growing number of effects such as carrier-carrier interactions, carrier degeneracy, quantum confinement [11–13] or even account for non-thermal distributions [14, 15].

Simultaneously, several experiments were conducted. First, continuous-wave photoluminescence (PL) was used to show that, in steady state, the *effective* temperature of the electron-hole plasma depends on the majority carrier type [16]. Then, the simultaneous use of continuous-wave PL and electrical mobility measurements allowed to distinguish the temperature of electrons and holes for the first time [17, 18]. This technique was however limited to doped samples and weak photogeneration regime. After these pioneer works in steady-state, electron and hole temperatures were mostly studied with time-resolved methods, including ultrafast time-resolved photoluminescence [19–23] and transient absorptivity spectroscopy [24–26]. In most cases, these authors reported that electrons were hotter than holes.

The challenging part of two-temperature measurements is that all the techniques described above are sensitive simultaneously to electron and hole distributions. To disentangle the contribution from each carrier, the authors usually rely on identifying spectral regions where the signal variation comes dominantly from only one carrier type. This typically requires heavily doped samples (as compared with photogeneration), as in the case of band-edge PL [21, 22], band-edge absorption [26] or electron-acceptor PL measurements [20]. Another possibility is to probe high-energy transitions with almost empty holes states, as is the case for electron-aligned off holes absorption measurements [25].

In this work, we propose the first experimental method to determine simultaneously electron and hole temperatures purely from continuous-wave PL measurements (see Sect. III). This technique relies on the precise determination of band-filling effect, described in Sect. III A. It is thus restricted to regimes of strong excitation, where the system is *close enough* to degeneracy (see Sect. III B).

* Institut Photovoltaïque d'Ile de France, UMR-IPVF 9006, CNRS, Ecole Polytechnique IPP, ENSCP PSL, Palaiseau, France.; Corresponding author: thomas.vezin.x15@polytechnique.edu

[†] Institut Photovoltaïque d'Ile de France, UMR-IPVF 9006, CNRS, Ecole Polytechnique IPP, ENSCP PSL, Palaiseau, France.

[‡] Université de Toulouse, INSA-CNRS-UPS, LPCNO, Toulouse, France

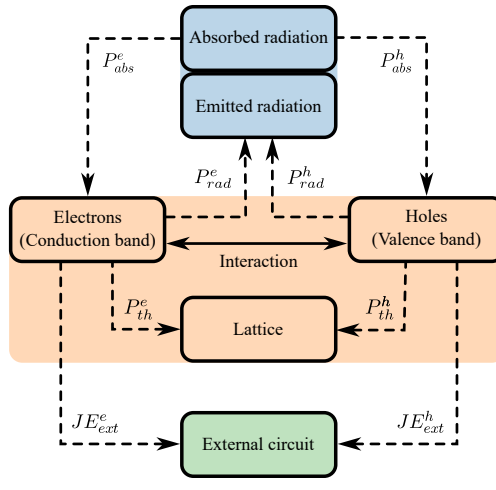


FIG. 1. Energy exchanges in a HCSC. Plain arrows indicate processes that tend to equilibrate electron and hole temperature, while dashed arrows tend to disequilibrinate it. Photons are represented in blue, while the HCSC is highlighted in orange and the external circuit is shown in green. In the parabolic band approximation for instance, it can be shown that $P_{\text{abs}}^e = (1 - \xi)P_{\text{abs}} + (1/2 - \xi)E_g\Phi_{\text{abs}}$, where P_{abs} (resp. Φ_{abs}) is the power (resp. photon flux) absorbed by the system, and $\xi = m_e/(m_e + m_h)$ is the mass mismatch. The other absorption and emission processes have similar expressions.

Note that this is not too restrictive for hot-carrier absorbers which are supposed to operate at strong excitation intensities. After introducing some methodological details in Sect. IV, we apply this 2-temperature measurement technique on PL spectra acquired from an InGaAsP single quantum well. We report electron temperatures above 1000 K at largest excitation intensity, while holes remain close to lattice temperature (see Sect. V). The increase in effective temperature – around 900 K – is found to be the largest ever measured in III-V materials at similar excitation intensity (see Sect. V B). In addition, hole heating is too large to be explained solely by photon absorption. This indicates that electron-hole interactions cannot be neglected in this system and calls for a better modeling of thermalization mechanisms in such two-temperature systems.

II. DESCRIPTION OF A TWO-TEMPERATURE SYSTEM

In this section, we recall few physical results on two-temperature systems (*i.e.* systems in which electrons and holes follow thermal distributions at different temperatures). In Sect. II A, we recall the law of emission of such a system. Then, in Sect. II B, we establish physical boundaries for electron and hole temperatures from simple energy considerations.

A. Two-temperature Generalized Planck Law

Light emission by a semiconductor is generally described by the Generalized Planck Law (GPL) [27], which considers that electrons and holes are at thermal equilibrium. Under the assumption of parabolic band for electrons and holes, this law can be generalized to the case where electrons and holes form thermal distributions of different temperatures [18, 28].

The photon flux emitted by the two-temperature system is described by the following equation (two-temperature GPL [28])

$$\Phi(E) = \frac{2\pi}{h^3 c^2} A(E) \frac{E^2}{\exp\left(\frac{E - \Delta\mu_{\text{eff}}}{k_B T_{\text{eff}}}\right) - 1} \quad (1)$$

where h is Planck constant, c is the speed of light in vacuum, k_B is Boltzmann constant. E is the energy of the emitted photon, $A(E)$ is the absorptivity of the system, and T_{eff} (resp. $\Delta\mu_{\text{eff}}$) is the effective temperature (resp. quasi-Fermi aligned QFLS) of the system.

The effective temperature and QFLS are defined as [28]

$$\begin{cases} \frac{1}{T_{\text{eff}}} = \frac{1 - \xi}{T_e} + \frac{\xi}{T_h} \\ \frac{\Delta\mu_{\text{eff}}}{k_B T_{\text{eff}}} = \frac{\mu_e}{k_B T_e} + \frac{\mu_h}{k_B T_h} - \frac{E_g}{k_B} \left(\frac{1}{2} - \xi\right) \left(\frac{1}{T_h} - \frac{1}{T_e}\right) \end{cases} \quad (2)$$

where $\xi = m_e/(m_e + m_h)$ is the effective mass mismatch and E_g is the bandgap of the absorber. Details about the energy convention used in this work can be found in Appendix A.

This shows that the PL spectrum of a two-temperature system can be described by a single effective temperature and a single effective QFLS. Thus, distinguishing T_e and T_h solely from this formula is impossible, as was pointed out by many authors [17, 21]. The key to simultaneous determination of T_e and T_h lies in the proper description of band filling (BF), as will be shown in Sect. III.

B. Physically available temperatures

Regardless of the method enabling two-temperature determination, we show here that a simple energy balance provides restrictive boundaries for the temperatures.

The energy brought by photon absorption is lost by (i) recombinations, which change the number of particles but not their mean energy, and (ii) thermalization, which draws carrier temperatures towards lattice temperature. Therefore, *in the absence of energy redistribution* between electrons and holes, electron and hole temperatures are bounded. They cannot be lower than the lattice temperature and the mean energy of each carrier must be smaller than the mean energy brought by photon absorption, as was shown by [28] for non-degenerate systems.

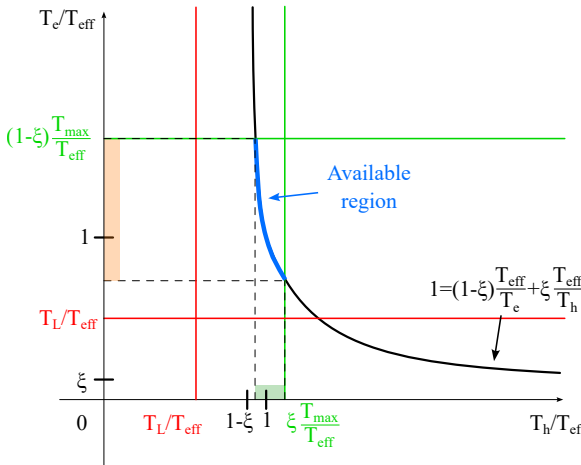


FIG. 2. Schematic representation of physical constraints on T_e and T_h for a given value of $T_{\text{eff}} \simeq 2T_L$ and $\xi \simeq 1/10$. Red (resp. green) lines show the lower (resp. upper) bound for electron and hole temperatures given by Eq. 3. Pale colors indicate the final interval allowed for T_e and T_h , in the same colors as in Fig. 6.

In addition, electron and hole temperatures are linked to the effective temperature by a hyperbolic relation (Eq. 2). For a given value of T_{eff} , the upper bound on T_h imposes a lower bound on T_e , and reciprocally. Overall, three different constraints apply on the carrier temperatures:

$$\begin{cases} T_L \leq T_e \leq (1 - \xi)T_{\text{max}} \\ T_L \leq T_h \leq \xi T_{\text{max}} \\ \frac{1}{T_{\text{eff}}} = \frac{1 - \xi}{T_e} + \frac{\xi}{T_h} \end{cases} \quad (3)$$

where T_L is the lattice temperature, $T_{\text{max}} = 2(\langle E_{\text{abs}} \rangle - E_g)/3k_B$ and $\langle E_{\text{abs}} \rangle$ is the average energy of absorbed photons.

This set of equations is depicted schematically in Fig. 2. The boundaries imposed by the two first equations are represented by green and red lines. Notice how the third relation constrains the values of T_e and T_h further than what was proposed in [28].

III. BAND FILLING MAKES TWO-TEMPERATURE DETERMINATION POSSIBLE

In this section, we present how it is theoretically possible to determine simultaneously electron and hole distributions from a single PL spectrum. At the high excitation rates necessary to produce hot carriers, the absorptivity $A(E)$ of the system depends on carrier populations through population-dependent effects such as BF, bandgap renormalization [29], exciton screening [30] or spectral linewidth broadening [31]. These population-dependent effects carry additional information on the carrier populations.

In particular, BF allows to distinguish electron and hole temperatures, as shown in Sect. III A. We then show that the two-temperature determination is accurate if and only if the system is *close enough* to degeneracy (Sect. III B) and provide a quantitative threshold for this regime.

A. Band filling

BF represents the change in absorption coefficient $\alpha(E)$ due to the non-negligible occupation of electron and hole levels close to their respective chemical potential. It writes [29]

$$\alpha(E) = \alpha_0(E) \times (1 - f_h(E_h) - f_e(E_e)) \quad (4)$$

where α (resp. α_0) is the absorption coefficient of the system in the presence (resp. absence) of BF, while E_e (resp. E_h) is the energy of the electron (resp. hole) involved in the absorption of a photon of energy E (see Fig. A.7).

A change in the absorption coefficient α may be visible on the PL spectrum through the absorptivity $A(E)$. For instance, if internal reflections and interferences in the sample can be neglected, Beer-Lambert law of absorption applies and $A(E) = (1 - R(E))(1 - \exp(-\alpha(E)d))$, with $R(E)$ the reflectivity of the layer and d its thickness.

Within the parabolic band approximation, $E_e = E_g/2 + (1 - \xi)(E - E_g)$ and $E_h = E_g/2 + \xi(E - E_g)$. If we assume in addition that electrons and holes follow thermal distributions, then the BF contribution writes

$$1 - f_h(E_h) - f_e(E_e) = \frac{\sinh\left(\frac{E - \Delta\mu_{\text{eff}}}{2k_B T_{\text{eff}}}\right)}{\cosh\left(\frac{E - \Delta\mu_{\text{eff}}}{2k_B T_{\text{eff}}}\right) + \cosh\left(\frac{1}{2}\left[\frac{E}{k_B}\left(\frac{1 - \xi}{T_e} - \frac{\xi}{T_h}\right) - \frac{\mu_e}{k_B T_e} + \frac{\mu_h}{k_B T_h} + \epsilon(T_e, T_h)\right]\right)} \quad (5)$$

with $\epsilon(T_e, T_h) = -\frac{E_g}{k_B}(\frac{1}{2} - \xi)(\frac{1}{T_e} + \frac{1}{T_h})$.

This BF contribution cannot be expressed only

in terms of effective temperature and QFLS. Therefore, the two-temperature GPL depends individually

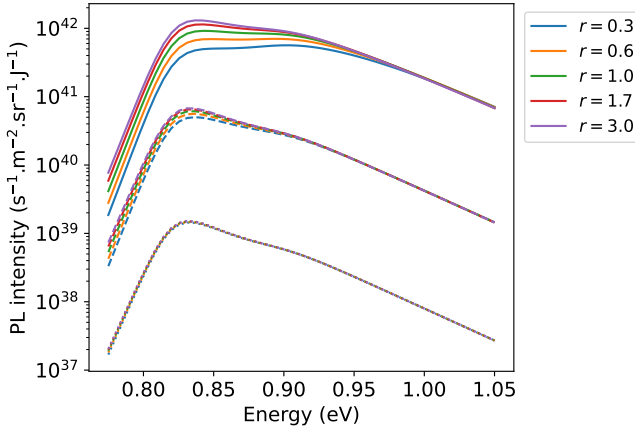


FIG. 3. Simulated PL spectra of an InGaAsP QW for different reduced QFLS ($\eta = -8$ (dotted), -4 (dashed) and 0 (plain)) and different temperature mismatch $r = T_e/T_h$, at $T_{\text{eff}} = 500$ K.

on T_e and T_h through the absorptivity term $A(E) = A(E, T_e, \mu_e, T_h, \mu_h)$.

B. Conditions to distinguish electron and hole temperature

To investigate theoretically the role of BF and of the independent temperatures of electrons and holes, we simulated PL spectra of the InGaAsP QW described in Sect. IV, using the absorptivity model presented in Sect. IV B and in Appendix B. Thanks to electroneutrality, it is possible to express the two-temperature GPL with only 3 variables instead of 4 (see Appendix C for details). In this section, we chose to use the effective temperature T_{eff} (see Eq. 2), the reduced QFLS η and the temperature mismatch r defined by

$$\begin{cases} \eta = \frac{\Delta\mu_{\text{eff}} - E_g}{k_B T_{\text{eff}}} \\ r = \frac{T_e}{T_h} \end{cases} \quad (6)$$

First, to visualize the effect of BF, we chose a constant value of the effective temperature $T_{\text{eff}} = 500$ K and simulated PL spectra using different values of the reduced QFLS and of the temperature mismatch. The result can be seen on Fig. 3. When the reduced QFLS is sufficient ($\eta \geq -4$ for instance), the spectra exhibit a clear dependence on r , which is visible in the low-energy part of the PL spectrum. In contrary, when the reduced QFLS is too low ($\eta \leq -8$ for instance), spectra with different temperature mismatch r can hardly be distinguished. This is simply because the system is not degenerate in this case, and therefore BF is negligible.

Then, we aim to establish a quantitative threshold for η above which two-temperature measurement is possible.

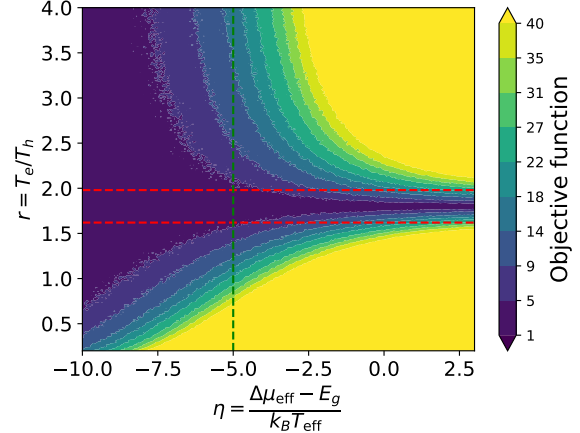


FIG. 4. Computed discrepancy between a reference spectrum with $T_{\text{eff}} = 500$ K and $r = 1.8$ ($T_e = 540$ K and $T_h = 300$ K) and spectra of varying r (y axis), as a function of the reduced QFLS (x axis). Horizontal dashed lines indicate the region $r = r_0 \pm 10\%$. Vertical dashed line indicates the threshold above which two-temperature determination is possible.

Let us say that we want to be able to distinguish variations of r of 10 % (arbitrarily). To do so, we need to compare the impact of a change of r to typical measurement noise, estimated to be an additive gaussian noise of mean 0 and deviation $\sigma = 2.5 \times 10^{-3} \times \max(I_{\text{PL}})$ for our PL setup.

We computed a collection of spectra at different values of η with a nominal value $T_{\text{eff}} = 500$ K and $r_0 = 1.8$. For every η , we computed the *discrepancy* between this nominal spectrum and a set of simulated spectra with different temperature mismatch $0.25 < r < 4$. This is represented on Fig. 4. The discrepancy is measured through an *objective function* defined in Sect. IV A and Appendix D.

When $\eta \leq -8$, the discrepancy between spectra with $1.5 \leq r \leq 3$ is less than the variations induced by noise, and different values of r cannot be distinguished. However, for $\eta \geq -5$, it becomes possible to distinguish spectra with $r = r_0 \pm 10\%$ (red dashed lines). This confirms our intuition that η must be "large enough" to ensure that we can distinguish two spectra with different temperature mismatch r . However, the precise value of the threshold depends on many arbitrary choices such as the desired precision on r , the shape of the spectrum, the choice of objective function, the noise level, etc. Therefore we estimate that the threshold above which two-temperature is feasible varies from $\eta \geq -7$ to $\eta \geq -3$ depending on the use case.

In conclusion, the key result of this section is that electron and hole temperatures may be distinguished from PL spectra if and only if the *QFLS is larger than a few $k_B T$ below the gap*.

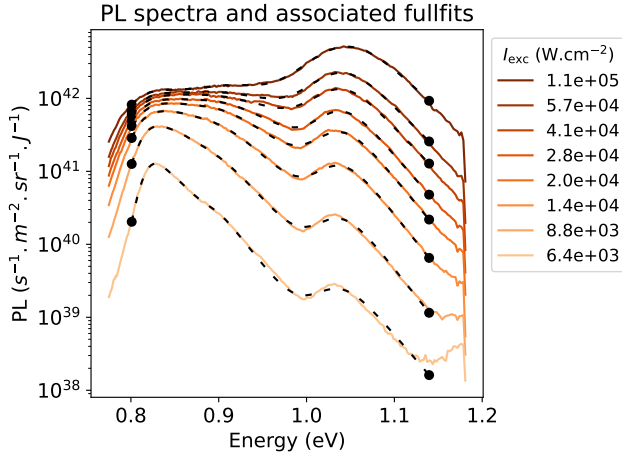


FIG. 5. PL spectra acquired at all power intensities. Dashed lines represent the result of a two-temperature full fit.

IV. EXPERIMENTAL AND METHODOLOGICAL DETAILS

In this section, we present in details the methodology to perform a two-temperature fit on continuous-wave PL spectra. Details on the sample and on the spectroscopy tools are given in Sect. IV A. The fit methodology is described in Sect. IV B, with an emphasis on the uncertainty assessment. Results and following discussion are presented in Sect. V.

A. Sample and experimental conditions

We applied our two-temperature determination technique on PL spectra from an $\text{In}_{.78}\text{Ga}_{.22}\text{As}_{.81}\text{P}_{.19}/\text{In}_{.8}\text{Ga}_{.2}\text{As}_{.435}\text{P}_{.565}$ single QW described elsewhere [32].

PL signal was collected with a NIR hyperspectral imager equipped with a Mitutoyo APO NIR x50 objective lens (0.41 NA). The excitation source is an Aerodiode 980 nm monomode laser focused to a Gaussian profile of radius 1.6 μm at 2σ . We studied only the most intense spectra obtained at the center of the illumination spot.

PL spectra were acquired with excitation intensities $6.4 \cdot 10^3 \leq I_{\text{exc}} \leq 1.2 \cdot 10^5 \text{ W.cm}^{-2}$. This corresponds to 64000 to 1.2 million suns, above the maximum concentration factor achievable for sunlight (46000) [33].

The PL spectra are shown on Fig. 5. QW emission can be seen around $E_g = 0.82 \text{ eV}$, with a secondary optical transition visible around $E_2 = 0.89 \text{ eV}$. The barrier emission can be seen above 1.05 eV. A clear change in slope at high energy in QW emission is indicative of hot carrier and BF effect, as will be explained below.

B. Two-temperature full fit methodology

a. Full fit. To take into account BF and other carrier-induced effects, we perform a *full fit* of the PL spectra [34]. This means that we model the absorptivity of the sample over the whole spectral range of PL emission, with a model inspired by [32].

The emission of the QW can be described by taking into account two energy levels for the QW, and one excitonic transition on its ground state. The contribution of BF in the QW is carefully assessed based on the 2-temperature model described in Sect. III B. For the barrier, a step-like absorptivity model is used. Since the barrier did not exhibit any significant hot-carrier effect, we used a single-temperature model to account for barrier BF.

Overall, the absorptivity model chosen to reproduce the PL spectra includes 18 different parameters (see Appendix B for details). By measuring the absorptivity through external quantum efficiency and by using electroneutrality relation, we are able to reduce to 10 the number of free parameters (see Appendix C for details).

b. Definition of the objective function. To perform a non-linear full fit, we need to define the *objective function* that will be minimized. For this two-temperature fit, two spectral regions of the QW emission are critical to obtain meaningful values of the fitting parameters. The first region is close to the bandgap, where electron and hole temperatures can be distinguished. The second region is where the absorptivity is almost constant (*i.e.* at high energy), such that it is easy to measure the effective temperature. To ensure that the regions are both accurately reproduced by the fit, we minimize an objective function defined piecewise as a linear norm at low energy ($E_{\text{LB}} \leq E \leq E_0$) and logarithmic norm at high energies ($E_0 \leq E \leq E_{\text{UB}}$). E_{LB} (resp. E_{UB}) is the lower (resp. upper) bound of the fitted energy range and E_0 is the energy distinguishing the two regions. See Appendix D.A for details.

V. RESULTS AND DISCUSSION

A. Two-temperature fitting results

We report the value of the fitted parameters as a function of the thermalized intensity in the well, $I_{\text{th}} = (E_{\text{las}} - E_g)/E_{\text{las}} \times I_{\text{abs},w}$ [35]. These results are summarized in Fig. 6. Errorbars account for possible overfitting and sensitivity to fitting conditions. They are computed based on a methodology described in Appendix D 2.

To estimate the thermalized power, we extrapolated an absorptivity $A(E_{\text{las}}) \sim 1 \%$ at the laser energy ($E_{\text{las}} = 1.265 \text{ eV}$, see Fig. C.8). Therefore, we assumed that $I_{\text{abs},w} \simeq 0.01 I_{\text{exc}}$. Note that a large uncertainty is associated with the determination of $I_{\text{abs},w}$, as a fraction of the power absorbed in the barrier ($I_{\text{abs},b} \sim 0.1 I_{\text{exc}}$) could also be injected in the well. We estimate that I_{th}

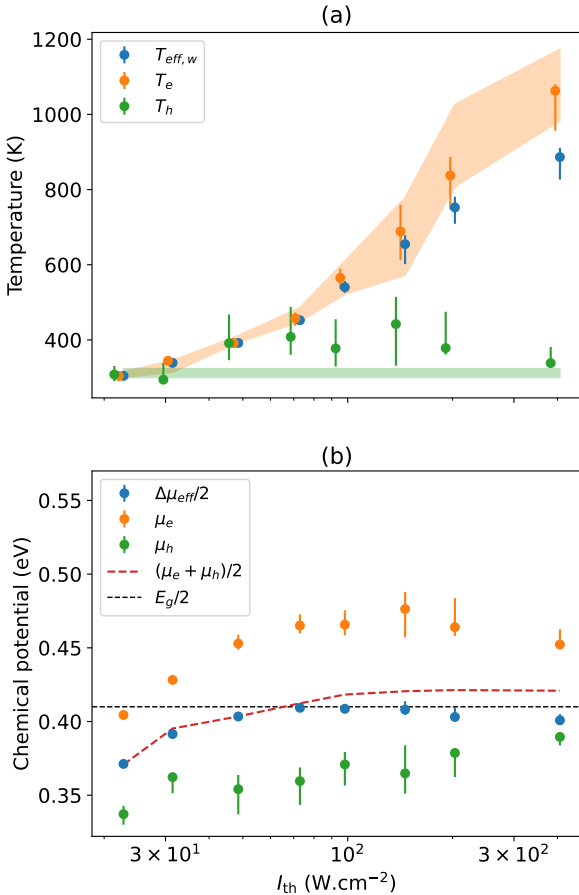


FIG. 6. From top to bottom (a) Temperatures extracted from the two-temperature full fit. Pale regions indicate the physically available temperatures obtained when neglecting electron-hole interactions (see Sect. II B). (b) QFLS and carrier chemical potentials corresponding to the same 2T full fits. Errorbars are computed following the methodology described in Appendix D 2.

could be up to two times larger than reported values. This uncertainty is not shown on Fig. 6 to avoid overloading the figure.

Carrier temperatures in the QW are displayed in Fig. 6a for increasing thermalized intensities. As intensity increases, the effective temperature increases from ambient to ~ 900 K. Similarly, electron temperature increases from ambient temperature to ~ 1000 K. However, hole temperature exhibits no clear trend and stays below 500 K at all intensities.

QFLS and carrier chemical potentials are represented in Fig. 6b. At low intensity $I_{\text{th}} \leq 10^2$ W.cm $^{-2}$, the QFLS and both chemical potentials increase for increasing intensity. However, at larger intensity, the QFLS and the electron chemical potential decrease. This decrease is associated with a large increase of both T_{eff} and T_e , such that carrier density is still increasing (see Fig. E.10).

Note that for most measured spectra, the electron chemical potential was above the bottom of the conduction band ($E_g/2$, black dashed line). Therefore electrons formed a degenerate system. However, holes stayed non-degenerate, as their chemical potential was few $k_B T_h$ below $E_g/2$.

B. Discussion

a. Are electrons and hole temperatures significantly different? For low thermalized powers $I_{\text{th}} < 80$ W.cm $^{-2}$, electron and hole temperatures are not distinguishable from the effective temperature due to large uncertainties. However, for larger thermalized powers $I_{\text{th}} \geq 80$ W.cm $^{-2}$, holes are found to be significantly colder than electrons. Note that for carrier distributions reported in Fig. 6, we find that $\eta \geq -3$ for all measured intensities. Therefore, we are in the regime in which two-temperature determination is possible *in theory* (see Sect. III B). However, as the uncertainty over T_e and T_h is around 100 – 200 K, it is not possible to distinguish them until T_{eff} surpasses 500 K, which happens only for intensities $I_{\text{th}} \geq 80$ W.cm $^{-2}$.

Our data suggests that electrons become hot, while holes remain colder, close to lattice temperature. Such a behavior has been reported by many authors studying other III-V materials, in steady-state [18, 36] and transient regime [10, 24].

Another proof that $T_e \neq T_h$ at high intensities comes from the effective QFLS. At intensities $I_{\text{th}} \geq 80$ W.cm $^{-2}$, the QFLS departs from the isothermal value, represented in a dashed red line in Fig. 6b. If the system could be described by a single temperature, then we would have $\Delta\mu_{\text{iso}} = \mu_e + \mu_h$. This is clearly not the case for high intensities, and the fact that $\Delta\mu_{\text{eff}} < \Delta\mu_{\text{iso}}$ implies that $T_e > T_h$ (see Eq. 2).

b. Hot-carrier effect and thermalization coefficients
The increase in effective temperature in hot-carrier absorbers is often characterized by a thermalization coefficient [35, 37–39]. However, thermalization models allowing for a simple characterization of materials exhibiting a different temperature for electrons and holes do not yet exist. In particular, hole temperature does not exhibit a clear trend with increasing excitation intensity (see Fig. 6a), and therefore cannot be explained by a model as simple as the ones presented in the articles cited above.

However, it should be noted that the InGaAsP QW measured in this article exhibits the largest effective temperature for comparable thermalized intensities [35, 37, 38, 40]. Therefore, this sample is one of the best III-V hot-carrier absorber ever characterized.

c. Energy exchange and boundaries Insight about energy exchanges in this system can be obtained by looking at physical boundaries for carrier temperatures. As stated in Sect. II B, when electron-hole interactions are negligible, T_e and T_h can only take restricted values. We

computed these physical boundaries for all fitted values of T_{eff} , and reported the result in pale colors in Fig. 6.

The fitted value of electron temperature (orange points) is always comprised in the physically available range (light orange region). However, holes are almost systematically hotter than allowed by those boundaries (light green region). This means that electron-hole interactions cannot be completely neglected.

A proper description of thermalization in this two-temperature regime could explain the heating of holes. Indeed, hot electrons are expected to generate many LO phonons, which can be absorbed by holes, resulting in a carrier-carrier energy transfer mediated by LO phonons.

Some other mechanisms for this energy redistribution (Coulomb interaction in particular) have been described theoretically [11] and evidenced experimentally [24] in time-resolved PL experiments. However, this study is the first evidence of such an energy redistribution obtained from continuous-wave PL.

VI. CONCLUSION

We proposed the first purely optical method to determine simultaneously electron and hole temperatures in steady-state. This technique relies on continuous-wave photoluminescence and more specifically on the precise determination of band-filling contribution. It can only be applied to systems close enough to degeneracy, but it should not be a limitation for hot-carrier absorbers, which are supposed to operate at large excitation intensities.

We successfully applied this technique on an InGaAsP single quantum well. We reported electron temperatures around 1000 K at largest excitation intensity, while holes remained close to lattice temperature. This sample exhibits the largest effective temperature – up to 900 K – ever measured in III-V hot-carrier absorbers with comparable thermalized intensities.

To further analyse this data, a proper thermalization model accounting for different carrier temperatures must be developed. This model will have to include energy transfers from electrons to holes in order to explain the increase of hole temperatures.

The fact that electrons and holes may not be at the same temperature in steady-state operation of a hot-carrier solar cell has implications in terms of hot-carrier solar cell design. Indeed, the optimal position of energy selective contacts depend on carrier temperature. In addition, the fact that electrons are hot while holes stay cold may impact the efficiency of the resulting hot-carrier solar cell. This will be investigated in future research.

ACKNOWLEDGMENTS

The authors would like to acknowledge the French National Research Agency, specifically the grant ANR ICE-

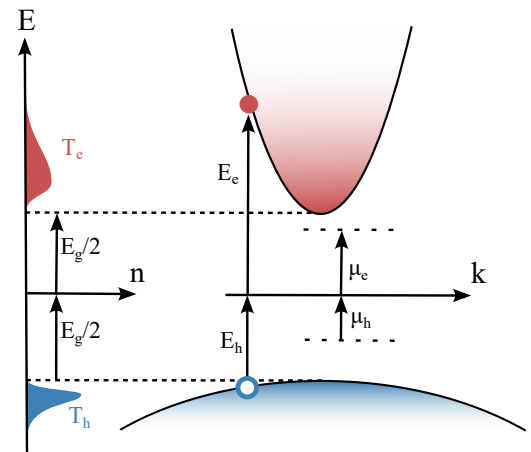


FIG. A.7. Schematic of a hot-carrier absorber band structure in the parabolic band approximation and energy conventions used in this work. Carrier densities are represented in the case where electrons are hotter than holes. Upward arrows indicate a positive quantity. Note how hole energies are measured with opposite sign as compared with electron energies.

MAN 19-CE05-0019-01, as well as PEARL program of IPVF for providing funds for this research. We especially thank FOTON Institute for providing the sample.

Appendix A: Energy convention used in this work

In a semiconductor, electrons in the valence band are often described as holes, *i.e.* vacancies in the valence band. By definition, holes have an opposite charge, opposite wave vector, opposite energy and opposite effective mass as compared with valence band electrons. For this reason, they are described by an occupation function

$$f_h(E_h) = \frac{1}{1 + \exp\left(\frac{E_h - \mu_h}{k_B T_h}\right)} \quad (\text{A1})$$

where $E_h = -E_{e,V}$ and $\mu_h = -\mu_{e,V}$ are the opposite of the energy of corresponding electrons in the valence band.

Fig. A.7 is a schematical representation of the energy conventions used in this work. If electrons and holes do not have the same effective mass, the absorption of a photon of energy E will not give the same energy to electrons and holes. Indeed, $E_e = E_g/2 + (1 - \xi)(E - E_g)$ and $E_h = E_g/2 + \xi(E - E_g)$ with ξ the effective mass mismatch (see main text).

Appendix B: Description of the absorptivity model

In this appendix, we describe the model used to describe and fit our photoluminescence (PL) spectra. In

the Generalized Planck Law, most of the difficulties in term of modelling come from the absorptivity A , which depends on many variables.

1. Description of a single layer

a. Absorptivity and absorption coefficient We have already explained in the main text that the absorptivity A of a single layer is linked to the absorption coefficient α by the Beer-Lambert law of absorption

$$A = (1 - R(E))(1 - \exp(-\alpha d)) \quad (\text{B1})$$

We take into account the effect of BF on the absorption coefficient [29].

$$\alpha(E) = \alpha_0(E) \times BF(E, T_e, \mu_e, T_h, \mu_h) \quad (\text{B2})$$

where α_0 is the absorption coefficient measured in the dark, and $BF = 1 - f_h - f_e$ is the contribution of BF (see Eq. 5)

Because we measured QFLS values close to the bandgap for both the quantum well and the barriers, we included this BF contribution in the absorption of both layers. We consider that, in the quantum well, $m_{e,w} = 0.042 m_0$, $m_{h,w} = 0.41 m_0$, while in the barrier, $m_{e,b} = 0.061 m_0$ and $m_{h,b} = 0.54 m_0$ [32]. $m_0 = 9.1 \times 10^{-31}$ kg is the mass of one electron.

b. Quantum well absorption coefficient Quantum wells have step-like density of states and therefore step-like absorptivity. In our case, two levels are sufficient to explain our PL spectra (see main text, Sect. IV A). It has been shown that, in such a QW, exciton states may also have a significant contribution to the PL emission, even at room temperature [30, 32]. Therefore, we model our quantum well absorptivity with 9 parameters ($A_x, E_x, \Gamma_x, A_1, R_y, \Gamma_1, A_2, E_2, \Gamma_2$):

$$\begin{aligned} \alpha_0^{QW} &= A_x \exp \left[- \left(\frac{E - E_x}{\Gamma_x} \right)^2 \right] \\ + A_1 &\frac{1}{1 + \exp \left[- \left(\frac{E - E_1}{\Gamma_1} \right) \right]} \frac{2}{1 + \exp \left(-2\pi \sqrt{\frac{R_y}{|E - E_1|}} \right)} \\ + A_2 &\frac{1}{1 + \exp \left[- \left(\frac{E - E_2}{\Gamma_2} \right) \right]} \end{aligned} \quad (\text{B3})$$

where E_i denote the position of the energy level i , A_i the amplitude of the transition and Γ_i is a broadening parameter. $R_y = E_1 - E_x$ is the Rydberg binding energy of excitons. Note that we took into account the Sommerfeld enhancement factor in the emission of the first level.

c. Barrier absorption coefficient For the absorptivity of the barrier layer, we use a phenomenological step-like absorption

$$\alpha_0^B = A_b \frac{1}{1 + \exp \left(- \frac{E - E_b}{\Gamma_b} \right)} \quad (\text{B4})$$

Note that it is not necessary to use a more advanced model for the barrier because we are solely interested in the carrier temperature *in the quantum well*, which is only weakly affected by the model used for the barrier emission. For this reason, we used a single-temperature model for the BF in the barrier.

2. Emission of a multilayer

In a multilayer, light emitted in a deep layer may be partially reabsorbed by shallower layers. By denoting \mathcal{A}_w (resp. \mathcal{A}_b) the internal absorptivity of the quantum well (resp. the barrier), we can write that [32]

$$I_{PL}(E) = \frac{2E^2}{h^3 c^2} \left\{ \frac{\mathcal{A}_w(1 - \mathcal{A}_b)}{\exp \left(\frac{E - \Delta\mu_w}{k_B T_w} \right) - 1} \right. \\ \left. + \frac{\mathcal{A}_b(1 - \mathcal{A}_w)(1 - \mathcal{A}_b) + \mathcal{A}_b}{\exp \left(\frac{E - \Delta\mu_b}{k_B T_b} \right) - 1} \right\} \quad (\text{B5})$$

Appendix C: Strategies to reduce the number of free parameters in our model

In total, our full fit model includes eighteen parameters. Six are related to the carrier distribution: in the well (T_e, μ_e, T_h, μ_h) and in the barrier ($T_b, \Delta\mu_b$). Twelve are related to the material ($A_x, E_x, \Gamma_x, A_1, E_1, \Gamma_1, A_2, E_2, \Gamma_2, A_b, E_b, \Gamma_b$). Those eighteen parameters being partially redundant, we need a strategy to reduce the risk of overfitting our data and obtain meaningful values for the carrier distribution parameters that we are most interested in.

1. Determining materials parameters with EQE

For the band-to-band transition, some of the material parameters remain constant when changing the excitation intensity. This is the case of the absorption amplitudes (A_1, A_2, A_b) and of the energies of the optical transitions (E_x, E_1, E_2, E_b). These *material parameters* may be determined from an absorptivity measurement. For instance, external quantum efficiency (EQE) measurement can be used to determine the low-power absorptivity $A = (1 - R)(1 - \exp(-\alpha_0 d))$, assuming that all photogenerated carriers are extracted in the contacts.

However, other parameters depend on the excitation regime and cannot be determined by this technique. For instance, the linewidths ($\Gamma_x, \Gamma_1, \Gamma_2, \Gamma_b$) are power-dependent because they depend on the phonon density [31]. Similarly, the exciton absorption peak A_x can be screened by increasing carrier density [30].

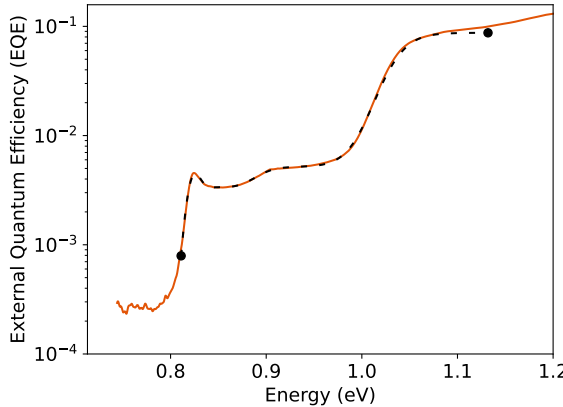


FIG. C.8. EQE spectrum obtained at room temperature, along with a fit using the absorptivity model described in the sections above.

Fig. C.8 shows the EQE spectrum measured with a ThermoFisher FTIR-FTPS using a 32 cm^{-1} resolution. It was fitted against an absorptivity model derived from Eq. B5, assuming that $T_w = T_b = 293 \text{ K}$ and $\Delta\mu_w = \Delta\mu_b \ll E_x$. Table I reports the fitted value of the seven material parameters, which were used to model all PL spectra.

Parameter	E_x	A_1	E_1	A_2	E_2	A_b	E_b
Value	0.823	$5.4 \cdot 10^5$	0.828	$7.4 \cdot 10^5$	0.890	$8.5 \cdot 10^5$	1.035

TABLE I. Absorption parameters determined by EQE measurement. Absorption coefficients are in m^{-1} while energies are in eV. These values were used to fit all PL spectra in this study.

Five more *power-dependent* parameters were necessary to reproduce the EQE spectrum, and are reported in Table II. These parameters depend on excitation intensity and on position, such that they were kept as fitting parameters for the PL spectra [32].

Parameter	A_x	Γ_x	Γ_1	Γ_2	Γ_b
Value	$6.5 \cdot 10^5$	0.007	0.005	0.011	0.013

TABLE II. Power-dependent absorption parameters necessary to reproduce the EQE spectrum. Absorption coefficients are in m^{-1} while spectral bandwidth are in eV. These parameters were fitted again for each and every PL spectrum presented in the main text, as they depend on carrier population.

2. Electroneutrality

The sample investigated here is intrinsic, and in a regime of strong photogeneration. Therefore, it can be assumed that there are as many electrons as holes in the

quantum well. Electroneutrality provides a relation between (T_e, μ_e, T_h, μ_h) , such that only three of them are independent.

$$\int_0^\infty dED_e(E)f_e(E, T_e, \mu_e) = \int_0^\infty dED_h(E)f_h(E, T_h, \mu_h) \quad (\text{C1})$$

where $D_i(E) \propto m_i^{D/2}(E - E_g/2)^{D/2-1}$ is the density of state of particles i , and D is the dimensionality of the absorber ($D = 2$ in our case).

In a QW, the density of states is a step-function. Here we assume that there are two energy levels E_1 and E_2 , and that they are symmetrical for electrons and holes. Therefore, Eq C1 can be integrated explicitly and rewritten as

$$\begin{aligned} & m_{e,w} T_e \sum_{i=1}^2 \log \left[1 + \exp \left(-\frac{E_i/2 - \mu_e}{k_B T_e} \right) \right] \\ & = m_{h,w} T_h \sum_{i=1}^2 \log \left[1 + \exp \left(-\frac{E_i/2 - \mu_h}{k_B T_h} \right) \right] \end{aligned} \quad (\text{C2})$$

Appendix D: Methodological details for the two-temperature full-fit

In this appendix, we provide details on the definition of the objective function that we minimized during the 2-temperature full fit (Sect. D 1). We then provide details on the uncertainty assessment (Sect. D 2).

1. Choice of objective function to minimize

a. Objective function definition In spectroscopy in general, and in hot-carrier community in particular, it is customary to fit PL spectra with a logarithmic scale. Indeed, a change in carrier temperature results in a change of the high energy slope, which is easily identified in log scale. Additionally, PL spectra span over several orders of magnitude, such that a linear scale would not be sensitive to spectral regions of low intensity, in particular the high energy part. Therefore, the usual objective function used to fit 1-temperature models is defined as

$$[d_{\log}(I_{\text{PL}}, I_{\text{PL}}^{\text{exp}})]^2 = \sum_{E_i} \frac{(\log I_{\text{PL}}(E_i) - \log I_{\text{PL}}^{\text{exp}}(E_i))^2}{N(\log I_{\text{PL}}^{\text{exp}})^2} \quad (\text{D1})$$

For the 2-temperature fit, the low energy part of the PL spectrum becomes very important. Indeed, it is the region in which one can observe the effect of BF and hence of the temperature mismatch between electrons and holes. A linear objective function would be more sensitive to small discrepancies of the temperature mismatch:

$$[d_{\text{lin}}(I_{\text{PL}}, I_{\text{PL}}^{\text{exp}})]^2 = \sum_{E_i} \frac{(I_{\text{PL}}(E_i) - I_{\text{PL}}^{\text{exp}}(E_i))^2}{N\langle I_{\text{PL}}^{\text{exp}} \rangle^2} \quad (\text{D2})$$

To combine the advantages of those two objective functions, we defined a composite objective function consisting of a logarithmic scale at high energy and a linear scale at low energy. The relative weight between those two regions is controlled by a hyperparameter λ :

$$[d(I_{\text{PL}}, I_{\text{PL}}^{\text{exp}})]^2 = \sum_{E_i \leq E_0} \frac{(I_{\text{PL}}(E_i) - I_{\text{PL}}^{\text{exp}}(E_i))^2}{N_{\leq} \langle I_{\text{PL}}^{\text{exp}} \rangle_{\leq}^2} + \lambda^2 \sum_{E_i > E_0} \frac{(\log I_{\text{PL}}(E_i) - \log I_{\text{PL}}^{\text{exp}}(E_i))^2}{N_{>} \langle \log I_{\text{PL}}^{\text{exp}} \rangle_{>}^2} \quad (\text{D3})$$

where N_{\leq} (resp. $N_{>}$) is the number of measurements points at energy lower (resp. greater) than E_0 , and $\langle \cdot \rangle_{\leq}$ (resp. $\langle \cdot \rangle_{>}$) is the average over the subset of points at energy lower (resp. greater) than E_0 .

b. Systematic comparison of the performances of these objective functions To compare between these different objective functions, we performed a 2-temperature full fit using each one of them. By varying the lower bound of the interval over which the fit is performed, we obtain an insight on how sensitive this fit is to external conditions. We compare the performances of the different objective functions by comparing the dispersion over the estimated carrier temperatures. For each spectrum, we compute the standard deviation over the determination of T_e (resp. T_h), and divide it by the average value of T_e (resp. T_h). Then we average this quantity over all PL spectra.

We varied E_{LB} from 0.77 eV to 0.83 eV, and kept $E_{\text{UB}} = 1.14$ eV. We set $E_0 = 0.90$ eV, in the middle of the quantum well emission. We used different values of the hyperparameter λ , ranging from 1 to 100. We also tried the pure linear and pure logarithmic objective function over $[E_{\text{LB}}, E_{\text{UB}}]$.

The comparison of the dispersion of all these objective functions is presented on Fig. D.9. It appears that the objective function with lowest dispersion is the pure linear one. However, we observed in many cases that this linear objective function tends to overestimate carrier temperatures by several tens of percent and therefore we chose to discard it. The next best objective function is the mixed one with $\lambda = 10$. Therefore we used this mixed objective function to fit the PL spectra presented in the main text.

2. Uncertainties assessment

Our 2-temperature full fit implies the determination of 10 different parameters for each spectrum. As the model is not linear in the parameters, they cannot be determined completely independently, and overfitting is a dominant error source. To assess the magnitude of this overfitting error, we performed a *sensitivity analysis* by repeating each fit several times with slightly different parameters than a *reference case*. For each repetition, we compared the fit goodness (i.e. the optimal objective function value) to the reference one, and considered the

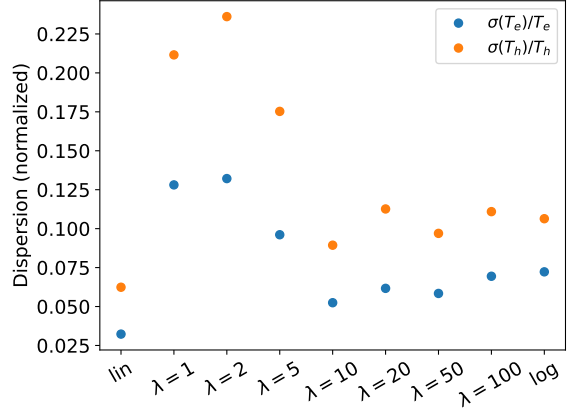


FIG. D.9. Dispersion over the estimated carrier temperature obtained with each objective function.

new fit acceptable if its fit goodness was not higher than 3 % above the reference. Since all these fits are equally acceptable, the uncertainty on the parameter determination was taken as the difference between the maximum and minimum value obtained in all the repetitions.

a. Reference case. The reference situation was obtained by setting the energy range for the fit to $E_{\text{LB}} = 0.80$ eV and $E_{\text{UB}} = 1.14$ eV. We also set the hyperparameter $\lambda = 10$ (see Appendix D 1). All 10 fitting parameters were completely free, although we forced the exciton absorption peak A_x to decrease and the spectral linewidths Γ s to increase with increasing excitation intensity [30, 31]. The resulting full fit is shown in Fig. 4.

b. Influence of the energy interval. The two-temperature determination is sensitive to the low-energy side of the PL spectrum. Therefore, we first studied the influence of the energy range by changing the lower energy bound E_{LB} in the range 0.80 ± 0.3 eV. We did not change E_{UB} as the low-energy region has a much greater impact on the determination of electron and hole temperatures.

c. Influence of the exciton screening. Then, we changed manually the magnitude of the exciton absorption peak A_x by ± 30 % around the value obtained in the reference situation. Indeed, BF and screening of the exciton absorption peak are both power-dependent effects which affect the low-energy part of the PL spectrum. Therefore their relative contribution are difficult to disentangle and this leads to increased uncertainty on the temperature determination.

Appendix E: Additional results of the two-temperature full fit

Carrier density is represented in Fig. E.10. As expected, carrier density increases with increasing excitation intensity.

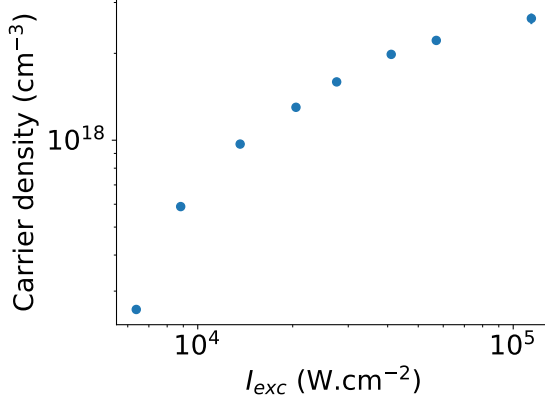


FIG. E.10. Carrier density in the QW as a function of thermalized power. Errorbars are too small to be seen.

Fig. E.11 presents the evolution of several fitting parameters with thermalized power.

Fig. E.11a represents the evolution of A_x , the exciton absorption peak. It shows that A_x is decreasing with increasing thermalized power, as it should [30]. Note that the dispersion on the determination of A_x is of several orders of magnitude. This illustrates the fact that A_x is largely unknown.

Note that for $I_{\text{th}} \geq 200 \text{ W.cm}^{-2}$, the uncertainty over A_x spans across several orders of magnitude. This is because, in this range, $A_x < 4 \times 10^4 \text{ m}^{-1}$, and therefore the effect of exciton absorption becomes negligible as compared with the emission from the ground state of the QW, characterized by $A_1 = 5.4 \times 10^5 \text{ m}^{-1}$ (see Table I). In this regime of strong excitation, the fitting algorithm can no longer fit A_x consistently as its effect is negligible. However, this is a good thing with respect to the two-temperature determination. The fact that excitonic contribution becomes negligible means that we can estimate the BF effect with higher accuracy. This is visible on the fact that temperature errorbars are smaller at high intensity on Fig. 6 (main text).

For the sake of completeness, we represent the evolution of the spectral linewidths Γ_x , Γ_1 and Γ_2 in Fig. E.11b. These linewidths tend to increase with increasing excitation intensity because of increasing phonon populations [31]. The large errorbars of Γ_x for $I_{\text{th}} \geq 200 \text{ W.cm}^{-2}$ also come from the fact that excitonic contribution is negligible in this regime.

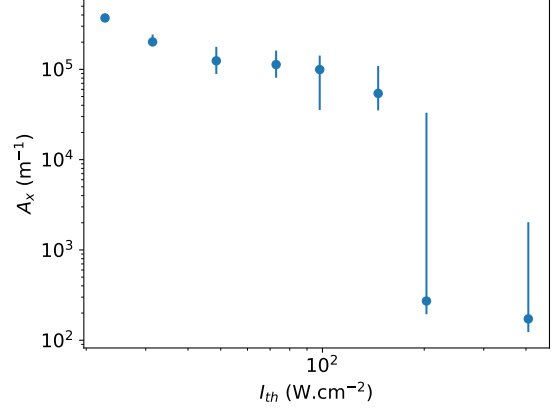


FIG. E.11. Evolution of (top) the exciton absorption peak and (bottom) the spectral linewidths of the QW with thermalized power. Errorbars are computed as explained in Sect. D 2.

- [1] R. T. Ross and A. J. Nozik, Efficiency of hot-carrier solar energy converters, *Journal of Applied Physics* **53**, 3813 (1982).
- [2] A. Othonos, Probing ultrafast carrier and phonon dynamics in semiconductors, *Journal of Applied Physics* **83**, 1789 (1998).
- [3] M. A. Green, Hot Carrier Cells, in *Third Generation Photovoltaics: Advanced Solar Energy Conversion*, Springer series in photonics (Springer, Berlin, Heidelberg, 2003) pp. 69–80.
- [4] Y. Rosenwaks, M. C. Hanna, D. H. Levi, D. M. Szmyd, R. K. Ahrenkiel, and A. J. Nozik, Hot-carrier cooling in GaAs: Quantum wells versus bulk, *Phys. Rev. B* **48**, 14675 (1993).
- [5] P. Würfel, Solar energy conversion with hot electrons from impact ionisation, *Solar Energy Materials and Solar Cells* **46**, 43 (1997).
- [6] A. Le Bris and J.-F. Guillemoles, Hot carrier solar cells: Achievable efficiency accounting for heat losses in the absorber and through contacts, *Applied Physics Letters* **97**, 113506 (2010).
- [7] S. Limpert, S. Bremner, and H. Linke, Reversible electron–hole separation in a hot carrier solar cell, *New J. Phys.* **17**, 095004 (2015).
- [8] B. K. Ridley, The electron-phonon interaction in quasi-two-dimensional semiconductor quantum-well structures, *J. Phys. C: Solid State Phys.* **15**, 5899 (1982).
- [9] S. A. Lyon, Spectroscopy of hot carriers in semiconductors, *Journal of Luminescence* **35**, 121 (1986).
- [10] M. Asche and O. G. Sarbei, The Role of Electron-Hole Interaction in the Cooling Process of Highly Excited Carriers, *physica status solidi (b)* **126**, 607 (1984).
- [11] K. Leo and J. H. Collet, Influence of electron-hole scattering on the plasma thermalization in doped GaAs, *Phys. Rev. B* **44**, 5535 (1991).
- [12] R. A. Taylor, C. W. W. Bradley, N. Mayhew, T. N. Thomas, and J. F. Ryan, Femtosecond hole burning measurements in semiconductors, *Journal of Luminescence* **53**, 321 (1992).
- [13] G. R. Hayes and R. T. Phillips, The effects of intervalley scattering on the cooling of hot carriers in In_{0.53}Ga_{0.47}As, *J. Phys.: Condens. Matter* **6**, 7589 (1994).
- [14] M. A. Osman and D. K. Ferry, Monte Carlo investigation of the electron-hole-interaction effects on the ultrafast relaxation of hot photoexcited carriers in GaAs, *Phys. Rev. B* **36**, 6018 (1987).
- [15] D. K. Ferry, M. A. Osman, R. Joshi, and M. J. Kann, Ultrafast relaxation of hot photoexcited carriers in GaAs, *Solid-State Electronics* **31**, 401 (1988).
- [16] J. Shah, A. Pinczuk, A. C. Gossard, and W. Wiegmann, Energy-Loss Rates for Hot Electrons and Holes in GaAs Quantum Wells, *Phys. Rev. Lett.* **54**, 2045 (1985).
- [17] R. A. Höpfel, J. Shah, and A. C. Gossard, Nonequilibrium electron-hole plasma in GaAs quantum wells, *Phys. Rev. Lett.* **56**, 765 (1986).
- [18] J. L. Pan, R. A. Hopfel, and J. Shah, Photoluminescence from GaAs quantum wells under high electric fields, *Journal of Applied Physics* **59**, 3925 (1986).
- [19] H. J. Polland, W. W. Rühle, J. Kuhl, K. Ploog, K. Fujiwara, and T. Nakayama, Nonequilibrium cooling of thermalized electrons and holes in GaAs/AlGaAs quantum wells, *Phys. Rev. B* **35**, 8273 (1987).
- [20] D. W. Snee, W. W. Rühle, Y.-C. Lu, and E. Bauser, Nonthermalized distribution of electrons on picosecond time scale in GaAs, *Phys. Rev. Lett.* **68**, 990 (1992).
- [21] A. Chebira, J. Chesnoy, and G. M. Gale, Femtosecond relaxation of photoexcited holes in bulk gallium arsenide, *Phys. Rev. B* **46**, 4559 (1992).
- [22] X. Q. Zhou, K. Leo, and H. Kurz, Ultrafast relaxation of photoexcited holes in n-doped III-V compounds studied by femtosecond luminescence, *Phys. Rev. B* **45**, 3886 (1992).
- [23] T. Gong, P. M. Fauchet, J. F. Young, and P. J. Kelly, Subpicosecond hot hole dynamics in highly excited GaAs, *Applied Physics Letters* **62**, 522 (1993).
- [24] C. W. W. Bradley, R. A. Taylor, and J. F. Ryan, Femtosecond electron and hole thermalisation in AlGaAs, *Solid-State Electronics* **32**, 1173 (1989).
- [25] A. Alexandrou, V. Berger, and D. Hulin, Direct observation of electron relaxation in intrinsic GaAs using femtosecond pump-probe spectroscopy, *Phys. Rev. B* **52**, 4654 (1995).
- [26] P. Langot, R. Tommasi, and F. Vallee, Nonequilibrium hole relaxation dynamics in an intrinsic semiconductor, *Phys. Rev. B* **54**, 1775 (1996).
- [27] P. Wurfel, The chemical potential of radiation, *J. Phys. C: Solid State Phys.* **15**, 3967 (1982).
- [28] F. Gibelli, L. Lombez, and J.-F. Guillemoles, Two carrier temperatures non-equilibrium generalized Planck law for semiconductors, *Physica B: Condensed Matter* **498**, 7 (2016).
- [29] B. Bennett, R. Soref, and J. Del Alamo, Carrier-induced change in refractive index of InP, GaAs and InGaAsP, *IEEE J. Quantum Electron.* **26**, 113 (1990).
- [30] D. S. Chemla, Two-dimensional semiconductors: Recent development, *Journal of Luminescence* **30**, 502 (1985).
- [31] H. Esmaeilpour, L. Lombez, M. Giteau, J.-F. Guillemoles, and D. Suchet, Impact of excitation energy on hot carrier properties in InGaAs multi-quantum well structure, *Progress in Photovoltaics: Research and Applications* **30**, 1354 (2022).
- [32] D.-T. Nguyen, L. Lombez, F. Gibelli, S. Boyer-Richard, A. Le Corre, O. Durand, and J.-F. Guillemoles, Quantitative experimental assessment of hot carrier-enhanced solar cells at room temperature, *Nat Energy* **3**, 236 (2018).
- [33] P. Wurfel and U. Wurfel, *Physics of solar cells: from basic principles to advanced concepts*, 3rd ed. (Wiley-VCH Verlag GmbH & Co. KGaA, Weinheim, 2016).
- [34] F. Gibelli, L. Lombez, and J.-F. Guillemoles, Accurate radiation temperature and chemical potential from quantitative photoluminescence analysis of hot carrier populations, *J. Phys.: Condens. Matter* **29**, 06LT02 (2016).
- [35] M. Giteau, E. de Moustier, D. Suchet, H. Esmaeilpour, H. Sodabani, K. Watanabe, S. Collin, J.-F. Guillemoles, and Y. Okada, Identification of surface and volume hot-carrier thermalization mechanisms in ultrathin GaAs layers, *Journal of Applied Physics* **128**, 193102 (2020).
- [36] V. R. Whiteside, B. A. Magill, M. P. Lumb, H. Esmaeilpour, M. A. Meeker, R. R. H. H. Mudiyanselage, A. Messager, S. Vijeyaraghavan, T. D. Mishima, M. B. Santos, I. Vurgaftman, G. A. Khodaparast, and I. R.

- Sellers, Valence band states in an InAs/AlAsSb multi-quantum well hot carrier absorber, *Semicond. Sci. Technol.* **34**, 025005 (2019).
- [37] A. Le Bris, L. Lombez, S. Laribi, G. Boissier, P. Christol, and J.-F. Guillemoles, Thermalisation rate study of GaSb-based heterostructures by continuous wave photoluminescence and their potential as hot carrier solar cell absorbers, *Energy Environ. Sci.* **5**, 6225 (2012).
- [38] L. Hirst, M. Yakes, C. Bailey, J. Tischler, M. Lumb, M. Gonzalez, M. Fuhrer, N. Ekins-Daukes, and R. Walters, Enhanced hot-carrier effects in InAlAs/InGaAs quantum wells, *IEEE J. Photovoltaics* **4**, 1526 (2014).
- [39] H. Esmaelpour, L. Lombez, M. Giteau, A. Delamarre, D. Ory, A. Cattoni, S. Collin, J.-F. Guillemoles, and D. Suchet, Investigation of the spatial distribution of hot carriers in quantum-well structures via hyperspectral luminescence imaging, *Journal of Applied Physics* **128**, 165704 (2020).
- [40] H. Esmaelpour, L. Lombez, M. Giteau, A. Delamarre, D. Ory, A. Cattoni, S. Collin, J.-F. Guillemoles, and D. Suchet, Investigation of hot carrier thermalization mechanisms in quantum well structures, in *Proc SPIE Int Soc Opt Eng*, Vol. 11681, edited by Freundlich A., Collin S., and Hinzer K. (SPIE, 2021).